

# Enabling Digital Twin for Bridge Deformation Analysis of Flash Flood Impacts: The Concept and Implementation Using DSLR Camera

Martinus Edwin Tjahjadi<sup>1,\*</sup>, Putu Harry Gunawan<sup>2</sup>, Hardianto<sup>3</sup>, Ester Priskasari<sup>4</sup>,  
Ketut Tomy Suhari<sup>1</sup>

<sup>1</sup>Department of Geodesy, National Institute of Technology (ITN) Malang, Indonesia

<sup>2</sup>CoE HUMIC School of Computing, Telkom University, Indonesia

<sup>3</sup>Department of Environmental Engineering, National Institute of Technology (ITN) Malang, Indonesia

<sup>4</sup>Department of Civil Engineering, National Institute of Technology (ITN) Malang, Indonesia

*Received December 26, 2024; Revised March 2, 2025; Accepted March 17, 2025*

## **Cite This Paper in the Following Citation Styles**

**(a):** [1] Martinus Edwin Tjahjadi, Putu Harry Gunawan, Hardianto, Ester Priskasari, Ketut Tomy Suhari, "Enabling Digital Twin for Bridge Deformation Analysis of Flash Flood Impacts: The Concept and Implementation Using DSLR Camera," *Civil Engineering and Architecture*, Vol. 13, No. 3, pp. 1820 - 1839, 2025. DOI: 10.13189/cea.2025.130328.

**(b):** Martinus Edwin Tjahjadi, Putu Harry Gunawan, Hardianto, Ester Priskasari, Ketut Tomy Suhari (2025). *Enabling Digital Twin for Bridge Deformation Analysis of Flash Flood Impacts: The Concept and Implementation Using DSLR Camera*. *Civil Engineering and Architecture*, 13(3), 1820 - 1839. DOI: 10.13189/cea.2025.130328.

Copyright©2025 by authors, all rights reserved. Authors agree that this article remains permanently open access under the terms of the Creative Commons Attribution License 4.0 International License

**Abstract** A sustainable maintenance of bridges is a very challenging task. Accurate information on the bridges' structure integrity could inform their lifespans. Meanwhile Digital Twins have emerged as transformative tools in monitoring and analyzing structures by creating virtual replicas of physical bridges to predict structural behaviors under various conditions. The integration of digital twin technology with bridge structures has revolutionized the field of structural maintenance. However, this technology has not been suited yet to accommodate the usage of DSLR cameras to monitor deformation which has been a day-to-day practice in photogrammetric community. This paper explores the concepts and implementation of performing bridge deformation monitoring using a DSLR camera by employing a novel statistical analysis. A case study was conducted by photographing a bridge concrete pillar in two different epochs. A convergent imaging network was applied to each photographing campaign to shoot around 33 retro target points attached to the pillar's surface. Ten photos on each epoch are processed using the least squares bundle adjustment to compute camera parameters and points of coordinates. This type of imaging network produces an orthogonal structure of the resulted covariance matrices of the 3D coordinates to simplify the statistical displacement analysis. The orthogonal and

homogenous covariance matrix structures simplify the congruency and localization test procedures. Also, a sub millimeter precision of the coordinate measurements is effortlessly attainable. It is revealed that there are insignificant structure movements occurring, and it has little implication of the bridge's internal structures. The study demonstrates the effectiveness of using DSLR cameras to enable digital twin to perform self-assessment mechanism to any deformation analysis on bridge structures.

**Keywords** Bridge Deformation, DSLR Camera, Surveying-Measurements, Photogrammetry, Structure Monitoring, Statistical Analysis, Digital Twin

---

## 1. Introduction

A sustainable maintenance of bridges from increasing frequencies and intensities of flash floods in Indonesia nowadays is a very challenging task. Accurate information on the bridges' structure integrity could inform their lifespans against such calamities. It has driven the adoption of technological advances in bridge monitoring

[1,2]. Among these, Digital Twin (DT) technology and Building Information Modeling (BIM) have emerged as innovative tools for monitoring, simulating, and addressing bridge deformation issues [3-6]. By integrating real-time data streams with detailed design and construction models, these technologies offer a holistic approach to managing challenges like structural deformations [3,4,7], environmental influences [8,9], and material aging [7,10,11].

Modern bridges face numerous stressors, such as mechanical loads, environmental changes, and operational wear. Heavy traffic, temperature fluctuations, and material degradation can lead to deformations that undermine structural integrity over time. Traditional inspection methods [12,13], while useful, are limited in capturing real-time changes or providing predictive insights essential for proactive maintenance [14,15]. This underscores the importance of DT and BIM integration, which facilitates a transition from reactive to predictive maintenance, ensuring long-term safety [16] and operational reliability [17].

DT utilizes IoT-enabled sensors to continuously monitor bridge performance, collecting data on stress, strain, vibration, and displacement [14,18]. This data is dynamically synchronized with virtual models, creating a live digital replica of physical structure. This synchronization enables real-time anomaly detection and assessment of structural behavior, empowering engineers to make informed maintenance decisions [2,19,20]. For instance, embedded sensors can alert engineers to excessive strain or material fatigue, enabling timely interventions to prevent failures [20].

BIM complements DT by providing a comprehensive database of a bridge's geometry, materials, and construction history, which forms the foundation for DT systems [5]. It facilitates multidisciplinary analysis by incorporating detailed material specifications and design elements, allowing for accurate simulations and context-driven maintenance decisions. This integration ensures maintenance actions are precise and effective, optimizing resource use [21].

Together, DT and BIM create a synergistic ecosystem for bridge deformation monitoring [14]. They enable real-time visualization and analysis of deformation patterns, enhance stakeholder collaboration through intuitive 3D models, and support efficient resource allocation [22]. Advanced computational techniques, such as finite element analysis (FEA) [2,23], finite element model (FEM) [21,23] and machine learning [24], leverage BIM's data alongside DT's real-time insights to predict structural responses under various scenarios, such as earthquakes or flash flood. Integration of DT and BIM ensures a sustainable approach to the safety, efficiency, and longevity of bridge structures [19,25].

Numerous bodies of literatures show that advances in various structures deformation monitoring methods [26–36]. These methods can be grouped into two distinct

approaches to measurement: physical context and geometrical context [28]. The physical context measures relative displacements in contact between instruments and the object [27,33]. Instruments that are used in these measurements are exceedingly high precision and it can provide continuous flow of monitoring [31] but it lacks intertwined information due to its local characteristic of observation [26,37,38]. In contrast, the geometric context can measure both absolute and relative displacements within a particular coordinate reference frame [36]. The absolute and relative monitoring networks are intuitively related to whether the observed target points are connected to stable reference points outside deformable body or all the detail points are subject to movement [39]. The stability of a given set of reference points to localize the point movement with respect to these reference ones that demand affirmative validation characterizes the absolute network. Meanwhile, in the relative one all points are subject to movement when the object changes in scale or shape [13,40]. The geometric context is widely used in both geodetic [29,30] and photogrammetric [32,34,35] related monitoring activities. However, both methods tend to absorb immaterial displacements into measurements that occurred only during time intervals between significant equilibrium [41,42]. Hence, more efforts are dedicated to accurately detecting and localizing significance displacements of detail points as it is a factual deformation rather than measurement deficiencies [43].

As a deformation measurement tool in geometrical context, a photogrammetric technique for structural monitoring has gained popularity since early 2000s for having a number of beneficial attributes such as the non-contact nature of the technique, the speed of photographing process utilizing numerous cameras, scalability and applicability techniques to objects of virtually any size, as well as flexibility and versatility of data processing system [35]. This technique relies on a limited set of discrete points on the structure's surface being photographed in consecutive times of monitoring [8]. These points are usually made of highly reflective materials to contrast them with the surrounding background material [44]. These points spatially relate the structure and the camera-images on each consecutive observation, hence 3D deformation of the structures can be analyzed. Any deviations of the points of coordinates between two consecutive epochs of measurements are subject to further deformation analyses [38–40].

This paper, therefore, elaborates a practical method and a robust statistical analysis of the deformable points to feed an existing DT or BIM model [45] to enable them to perform self-analysis [46] of the deformation of the points by utilizing the DSLR camera only [45,46]. Albeit geometric analysis is understandable, nonetheless a complexity of its localization of the deformable points cannot be hindered from the viewpoint of ordinary users, novel and straightforward approaches are warranted.

Hence, it aims to give expositions of any structure deformation through analysis of the coordinate differences of the modeled retro target markers on the DT from different measurement epochs. The findings will contribute to more resilient and sustainable infrastructure solutions, addressing critical challenges in modern bridge management.

## 2. Materials and Methods

Bridges form vital links for transportation networks in Malang Municipality – East Java province, Indonesia. Increasingly unpredicted monsoon rains recently have made flash flood occurrences to be more frequent which might inflict the bridges' structural integrity. Located on Pandansari village, the bridge has four main concrete pillars topped up with steel beams and hot-mix asphalts which span around 75m long. Such weather extremes raise concern about the bridge's two erected concrete pillars located on the riverbed which are directly exposed to the flood streams (Fig. 1). Visually spotted miniscule fractures on the pillars had been identified before the campaign began and they were subjected to investigate about a possibility of structure displacements. To ascertain the durability of the deteriorating pillars' structures and the lifespan of the bridge, deformation monitoring surveys were conducted. A photogrammetric deformation survey of selected portions of the pillars was undertaken to monitor the flash flood-inducing movements to millimeter accuracy over the course of two months at the very occasion of the flood's aftermath.

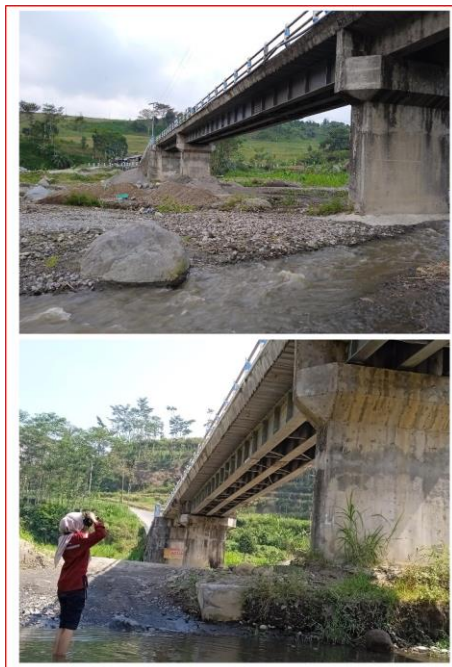


**Figure 1.** Deformation monitoring of bridge pillars using a DSLR camera

### 2.1. Structure Measurements

A photogrammetric deformation survey of selected portions of the pillars was undertaken to monitor the flash flood-inducing movements utilizing a DSLR camera. The survey was conducted at least two consecutive epochs at prior and aftermath events. A general workflow of the methodology is categorized into two main parts, namely point measurements and deformation analyses processes as depicted in Fig. 2. The process starts with a reconnaissance survey to provide early assessments about the bridge structure integrity and possibly difficulty level encountered when photographing the structures.

#### 2.1.1. Bridge Digital Twin Development

DT/BIM model encodes and links physical objects with its digital representation that can encrypt real-time phenomenon into the model for further analysis. The generation process of the model starts by photographing the bridge to render a 3D perspective view [47]. A detailed process is highly dependent on the application, typically involved seven distinct steps as follows [47]. First, triangulation of the structure surface with triangular facets to ensure that visualization can be rendered at the desired rates [48]. Next, integration of the facet meshes and linear features into the surface to ensure that no gap between the meshes and surfaces occur and that feature geometries are realistic [47]. Next, texture the structure surface using orthorectified images appropriate to the surface type, then insert geospatial information for the exact appearance of the surface model or spatially aware model [49]. The last three steps commence with generation of levels of details (LoD). That is a reduced resolution version of the model for use when the structures are far from the viewpoint [7]. Rendering the meshes can be speeded up by reducing the number of triangular polygons in distant parts of the scene where they would not be visible [50].

After that, the processed data was written into an interchangeable, run-time database format for rapid access to the information designed for visualization and simulation [51]. Finally, 3D scene rendering is performed by projecting each part of the scene to the desired viewpoint. The geometric, topological, semantic, and appearance properties are defined for each class of the LoD of the scene [7]. Deformation analysis results could be attached to each LoD component properties above [52] to describe range of complexity of the displacements that occur, allowing reasoning about more complex forces involved.

#### 2.1.2. Network Design and Measurements

The next stage on point measurement according to Fig. 2 is the imaging process of the specially designed markers attached to the bridge's pillar surface of susceptible parts of the structure undergoing deformation (Fig. 1). There is a certain rule of thumb when photographing structures to optimize results. A convergent network design of DSLR camera photography in capturing pillar's images optimizes

observation capability in terms of accuracy and efficiency [53]. This is quite a perplexing issue, especially when aspects of system self-calibration in the next photogrammetric restitution stage are involved (Fig. 2), which can influence the measurement accuracy of the camera [54].

Measuring accuracy is a function of the angular measurement resolution (i.e. CCD/CMOS sensor’s pixel size) and the geometry of intersecting rays at each target point (i.e. parallax angle). Angular measurement capabilities of the DSLR camera are quantified as the angle subtended over the camera focal length by the standard error of image coordinate measurements [55]. Fraser [53] formulates initial indicator of the coordinates of target points in convergent imaging networks as follows:

$$\bar{\sigma}_c = \frac{q}{\sqrt{k}} S \sigma = \frac{q}{\sqrt{k}} d \sigma_a \quad (1)$$

Where S is the scale given as a division between mean camera to object distance of d and the camera nominal focal length of c;  $\bar{\sigma}_c$  is the RMS value of standard-error of 3D coordinate of object points;  $\sigma$  and  $\sigma_a$  are standard

error of the image coordinate and standard error of the corresponding angular measurement respectively; q is design factor expressing the strength of figure of the imaging networks; and k is the average number of camera exposures at or near each station. Under the assumption the pillar façade occupies the full image frame, the (1) can be rewritten as follows [53]:

$$\frac{\bar{\sigma}_c}{R} = \frac{q}{\sqrt{k}} \frac{\sigma}{r} \quad ; \quad R = S \cdot r \quad (2)$$

Where R is the scene dimension in object space, the r is the image format dimension, and (2) provides a handy indicator of the 3D target point coordinate accuracy. A practical predetermined value of k = 1 and q = 0.7 is sufficient representation of strong geometry of imaging network. The scale value of  $\bar{\sigma}_c/R$  gives a measure of the accuracy capabilities of the DSLR camera measurement system, and it is obviously seen that multiple exposures at one station location improve object structure measurement precision [56]. For example, in this research, the precision of image measurements of pillar structures surpasses the imaging scale of about 1:67000.

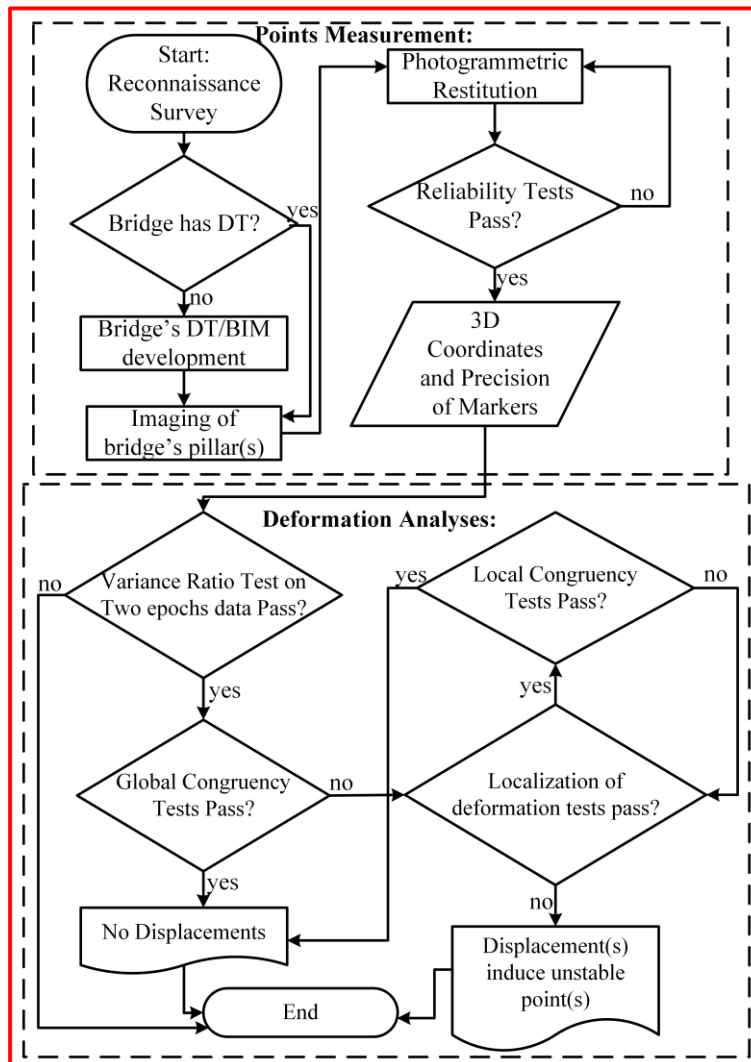


Figure 2. Schematic Methods on bridge deformation monitoring using a DSLR camera

### 2.1.3. Photogrammetric Restitution

Photogrammetric restitution (Fig. 2) is a process of computing photogrammetric exterior orientation (EO), interior orientation (IO), camera-lens distortion parameters, and 3D coordinate of marker points on the pillar façade simultaneously from the photographed images. While the EO parameters inform about the object space position of each camera when taking the picture, the IO as well as camera-lens distortion parameters provides transformation mechanisms of rays from the object space into the camera space and vice versa to quantify the precision of image measurements and the accuracy of the coordinate of measured 3D target points on the pillar's façade which are the ultimate goals of this process. A well-known collinearity model makes up the mathematical basis as follows.

$$x' = x - x_0 + \Delta x = -c \frac{R_1}{R_3} \quad (3)$$

$$y' = y - y_0 + \Delta y = -c \frac{R_2}{R_3} \quad (4)$$

$$c \frac{R_1}{R_3} = c \frac{r_{11}(X-X_c) + r_{12}(Y-Y_c) + r_{13}(Z-Z_c)}{r_{31}(X-X_c) + r_{32}(Y-Y_c) + r_{33}(Z-Z_c)} \quad (5)$$

$$c \frac{R_2}{R_3} = c \frac{r_{21}(X-X_c) + r_{22}(Y-Y_c) + r_{23}(Z-Z_c)}{r_{31}(X-X_c) + r_{32}(Y-Y_c) + r_{33}(Z-Z_c)} \quad (6)$$

Equations (3) and (4) illustrate an extended collinearity transformation from object or structure point (X, Y, Z) to a distortion free image point (x', y') through the camera's perspective center (X<sub>C</sub>, Y<sub>C</sub>, Z<sub>C</sub>) shifted by principal distance of *c* in (3) and (4) which implied a lens departure correction (Δ*x*, Δ*y*) of the observed image point (x, y). The *x*<sub>0</sub> and *y*<sub>0</sub> are the principal point coordinates to account for a perturb model of the projective equations. The principal distance and the principal point make up the IO parameters.

The DSLR camera lens comprises a system of optical parts affected by various errors due to certain limitations in the manufacturing processes. Imperfection of the lens components, for example, a departure from the prescribed refractive index of the glass used or imperfection in polishing, as well as minute errors in the centering of the individual lens elements and their placement as an entity in the camera makes up a major source of errors by perturbing the projective equations of (3) and (4) [57]. Physically interpretable departures can be grouped into a symmetrical radial distortion, decentering distortion, and affinity [58]. The first two of them cause main perturbation that can induce a failure of the lens to image a straight line in object space as straight line in image space, and cause image displacements, which directly affect the geometric accuracy of the object 3D points of coordinates [58].

The radial distortion displaces an image point radially towards or away from the image's principal point, from the supposedly ideal location to the actual image with positive values indicating outward displacements. This distortion is modelled using polynomials of *K*<sub>1</sub>, *K*<sub>2</sub>, and *K*<sub>3</sub> in (7) and (8) to uncompensated Seidel aberrations [59]. The decentering distortion of *P*<sub>1</sub> and *P*<sub>2</sub> in (7) and (8) is due to imperfect

alignment of lens elements to the camera's lens optical axis of the entire lens system at the time of manufacture [55]. This imperfection causes a shifting of the bundle of rays passing through the lenses to intersect the image plane at points away from the theoretical position. The *b*<sub>1</sub> and *b*<sub>2</sub> in (7) comprise the in-plane distortion parameters that account for differential scaling between the horizontal and the vertical pixel spacing and the non-orthogonality or non-skewness between the *x* and *y* axes of the camera's CCD or CMOS sensor plane. These distortions are uncompensated accordingly as follows:

$$\Delta x = -\frac{\bar{x}}{c} \Delta c + \bar{x} r^2 K_1 + \bar{x} r^4 K_2 + \bar{x} r^6 K_3 + (2\bar{x}^2 + r^2) P_1 + 2P_2 \bar{x} \bar{y} + b_1 \bar{x} + b_2 \bar{y} \quad (7)$$

$$d\Delta y = -\frac{\bar{y}}{c} \Delta c + \bar{y} r^2 K_1 + \bar{y} r^4 K_2 + \bar{y} r^6 K_3 + 2P_1 \bar{x} \bar{y} + (2\bar{y}^2 + r^2) P_2 \quad (8)$$

$$r = \sqrt{\bar{x}^2 + \bar{y}^2} = \sqrt{(x - x_0)^2 + (y - y_0)^2} \quad (9)$$

Equations (7) and (8) describe the total error budget of the displaced image point due to lens distortion, and Δ*c* is a correction to the principal distance, as well as *r* is radial distance of the displaced point from the image's principal point. The transformation of (3) and (4) determines a correspondence between the point in the object space and the idealized image point. The perturbed distortions of them are added to the observed image point locations.

The self-calibrating method, on the other hand, calibrates not the camera, but the photographed digital photos, so that the camera can be used immediately like normal shooting in the field. Calibrated photos come from captured images that have been corrected mathematically based on the principles of collinearity theory [60]. This theory states that the distortion contained in the lens and the noise contained in the CCD/CMOS sensor will bend the rays reflected from the object that passes through the lens and is received on the surface of the sensor plane [55]. If there were no distortion and noise on the camera, then this ray would be a straight line. Based on this postulate, if the straightness of the passing ray can be mathematically reconstructed in the imaging sensor, the distortion-free and noiseless images can be produced, termed as calibrated images. They can be grouped into two types. The first is an image that has been physically corrected through a digital rectification process. The other one is not physically rectified, but any spatial dissemination over uncalibrated image occurs, it must first be corrected for distortion and noise model that had been calculated. This research uses the second method of reading photo coordinates for feature points on the structures being photographed.

Object points on a pillar façade depicted in Fig. 3 are the prime focus for enabling displacement inspection of the structures. The dimensions of the pillar are around 6 meters wide and 16 meters tall. On the facade the pillar (Fig. 3), adhesive retro reflective target stickers which have very high light reflectance are attached, so they will appear sharper and have more contrast to the surrounding objects

when viewed in the photo. The use of this sticker is as an observation point of the pillar structure. Using convergent imaging geometry, photos of observable points were captured in two different epochs spanning over three-month period. The DSLR camera has of APSC sensor size.



**Figure 3.** Around 120 retro targets attached to the pillar facade

When employing the camera, compensation for removal of systematic image distortion is mandatory to achieve highly accurate 3D coordinates of these points. Compensating these errors is done by utilizing a camera self-calibrating bundle adjustment method [61]. The  $\Delta x$  and  $\Delta y$  in (7) and (8) are introduced to describe the behavior of these systematic errors and involved into the adjustment method a design matrix of  $A_3$  in (10). The basic of bundle adjustment method in (10) is expressed by the functional model of the  $\Delta x$  and  $\Delta y$ . Conceptually they consist of the total systematic error budgets and are expressed as follows.

$$\begin{matrix} \mathbf{A1}_{ij} & \delta 1_i & + & \mathbf{A2}_{ij} & \delta 2_j & + & \mathbf{A3}_{ij} & \delta 3_p & - & \mathbf{l}_{ij} & = & \mathbf{v}_{ij} \\ (2mn, 6m) & (6m, 1) & & (2mn, 3n) & (3n, 1) & & (2mn, p) & (p, 1) & & (2mn, 1) & & (2mn, 1) \end{matrix} \quad (10)$$

The  $i$  and  $j$  subscripts point to an index of the  $i^{th}$  image out of the  $m$  overlapping images used in the computation, and the  $j^{th}$  conjugate point out of the  $n$  object points on the object structure, and  $p$  is the number of lens distortion parameters. Vector  $\mathbf{v}$  is an observation residual in image coordinate measurements. Vector  $\mathbf{l}$  is a discrepancy between observations and approximations of the measured image coordinates. The matrices of  $\mathbf{A1}$ ,  $\mathbf{A2}$ ,  $\mathbf{A3}$  and their associate vectors of  $\delta 1, \delta 2, \delta 3$  are matrices of partial derivatives of parameters and vectors of correction terms to starting values respectively. The  $\mathbf{A1}$  and  $\delta 1$  are related to

extrinsic parameters, where  $\mathbf{A2}$  and  $\delta 2$  as well as  $\mathbf{A3}$  and  $\delta 3$  correspond with the object points coordinates and lens distortion as well as intrinsic parameters respectively. The solution of adjustment computation is written as:

$$\begin{bmatrix} \dot{N}_{ij} & \tilde{N}_i & \bar{N}_{ij} \\ \tilde{N}_i^T & \tilde{N}_k & \tilde{N}_j \\ \bar{N}_{ij}^T & \tilde{N}_j^T & \dot{N}_{ij} \end{bmatrix} \begin{bmatrix} \delta 1 \\ \delta 2 \\ \delta 3 \end{bmatrix} + \begin{bmatrix} \dot{C}_i \\ \check{C}_p \\ \check{C}_j \end{bmatrix} = 0 \quad (11)$$

$$\dot{N}_{ij} = \sum_{j=1}^n \mathbf{A1}_{ij}^T P_{ij} \mathbf{A1}_{ij} \quad (12)$$

$$\tilde{N}_{ij} = \sum_{i=1}^m \mathbf{A2}_{ij}^T P_{ij} \mathbf{A2}_{ij} \quad (13)$$

$$\tilde{N}_k = \sum_{i=1}^m \sum_{j=1}^n \mathbf{A3}^T P_{ij} \mathbf{A3} \quad (14)$$

$$\bar{N}_{ij} = \mathbf{A1}_{ij}^T P_{ij} \mathbf{A2}_{ij}; \tilde{N}_i = \mathbf{A1}_{ij}^T P_{ij} \mathbf{A3} \quad (15)$$

$$\hat{N}_j = \mathbf{A3}^T P_{ij} \mathbf{A2}_{ij}; \dot{C}_i = \sum_{j=1}^n \mathbf{A1}_{ij}^T P_{ij} w_{ij} \quad (16)$$

$$\check{C}_j = \sum_{i=1}^m \mathbf{A2}_{ij}^T P_{ij} w_{ij} \quad (17)$$

$$\check{C}_p = \sum_{i=1}^m \sum_{j=1}^n \mathbf{A3}^T P_{ij} w_{ij} \quad (18)$$

The weight matrixes of  $P$  and  $w$  in (12) – (18) relate coordinate observations as well as discrepancy term between approximation and observation respectively. Meanwhile, the  $\dot{N}$ ,  $\tilde{N}$  and  $\bar{N}$  submatrices are symmetric, block diagonal, with each block on the diagonal referring to the image's EO parameter in  $\dot{N}$ , the coordinates of object target point in  $\tilde{N}$ , and the IO and lens distortion parameters in  $\bar{N}$ . These matrices are developed by summation process as seen in (12) – (18).

The computational starting values of the EO parameters are calculated by using closed-form methods of space resection [62] and relative orientation [63] processes. This step is necessary since the observation of equations is non-linear with respect to the parameters. An iterative process of least squares bundle adjustment is proceeded by constructing the normal equation matrices. Solution of the equation is illustrated in [55,64,65]. Solving this equation requires convergent imaging geometry to recover the principal distance of  $c$  and the principal points offset of the camera. If (11) is further simplified into  $N\delta + C = 0$ , and  $C_x = \sigma_0^2 N^{-1}$  is the covariance matrix of the parameters, the  $C_x$  is utilized to ascertain the quality of the measured 3D points. It contains all the information necessary to define the precision of object points, camera orientation and location, as well as additional parameters of camera lens distortions.

This computation was carried out using open source-based software. The calculation process begins with registration process for the retro-target points. In every epoch, it produces a set of 3D coordinates of the target points and the camera calibration parameters. These parameters are utilized to calculate the calibrated 3D coordinates of the points in the object space system from overlapping images. The imaged 2D point on the digital images and their corresponding 3D point in the object space make up a pair of the point coordinates. There will be a one-to-one relationship of the constructed line of rays between them. It is known that uncompensated systematic

errors bend the straightness of the line, and it inflicts spatial accuracy of the pair location as illustrated in Fig. 4.

The remaining and uncompensated systematic errors are depicted as 2D circles or ellipses on the photo surface and as 3D circles or ellipses on the pillar object as seen in Fig. 4. The larger the diameter of the circle/ellipse indicates the greater the impact of the systematic error. In other words, the smaller the size of the circle/ellipse, the more accurate the coordinates of the 3D target point. For the perfect camera conditions, both systematic errors will no longer exist. These systematic errors affect the accuracy of the coordinates of the 3D points on the pillars. Therefore, when these errors can be quantified by self-calibration process, the precision of the derived coordinates of the points is instantly known, and they can be set as a tolerable limit to subjugate a determinable minimum of displacement value.

To sum up, the self-calibrating bundle adjustment method presents a practical means of achieving compensation for residual systematic errors in image space coordinates regardless of whether they arose from camera calibration errors or other physical perturbations within the imaging process. The method has made feasible 3D measurements to moderate to high accuracies from the DSLR camera. From the empirical experiments, it clearly shows that there are four main requirements for successful result in detecting displacements: first, implementation of a multi-image network configuration with moderate to highly convergent images; second, an involvement of orthogonal camera roll angles; third, good coverage and distribution of target points on the image format; last, a suggestion that a minimum of six images and 25 target points per image would sufficient for providing high observational redundancy.

## 2.2. Deformation Analyses

Given the postulate about a minimum detectable systematic error aforementioned, the smallest amount of possible displacement that can be identified and localized is about the same order of magnitude as the precision measurement of the camera [8]. The deformation analyses

play crucial role in providing geometrical-status information on the structure being monitored as well as an insight into the physical state of deformable body [66]. Hence, ensuring that all 3D point measurements are not contaminated with gross errors, random errors, and systematic errors is prerequisite for the process of the identification and localization of the displacements. A proof of the existence or non-existence of them is a central to any deformation analyses, since neither “true” coordinates nor “true” displacement” can be sensed through the camera [66]. The DSLR camera measures coordinates of the target points to infer changes in shapes, dimensions, and position in the 3D Cartesian reference system. To quantify the changes between two epochs of measurements, this paper utilizes a relative reference network [67] that all target points are assumed to be subject to movement when the pillar structure changes in shape or scale. The network aims to localize object target point movements which exceed preset tolerance.

### 2.2.1. Concept of Statistical Tests: Hypothesis Tests on Deformation Model

Equation (11) is an over-determined model which comprises functional and stochastic relationships based upon hypothetical observations of emanating bundle of rays from object target passing through the camera lenses to the sensor as seen in Fig. 4. The coordinates of the target points derived from (11) as well as other parameters have always been subject to essential consideration on how the model conforms with reality [69]. Algorithms in (11) enable the camera to measure 3D coordinates of the target points. A verification of the 3D coordinates parameter of (11) is very important [70] since errors in the model directly inflict the accuracy of the 3D coordinates of which tend to be interpreted as displacements in deformation analysis and may result in misleading conclusions. Statistical testing is the most favorable and applicable method in photogrammetric and surveying practitioners to utilize in minimizing bias interpretations [71], and it is introduced here to clarify discussions in the following sections.

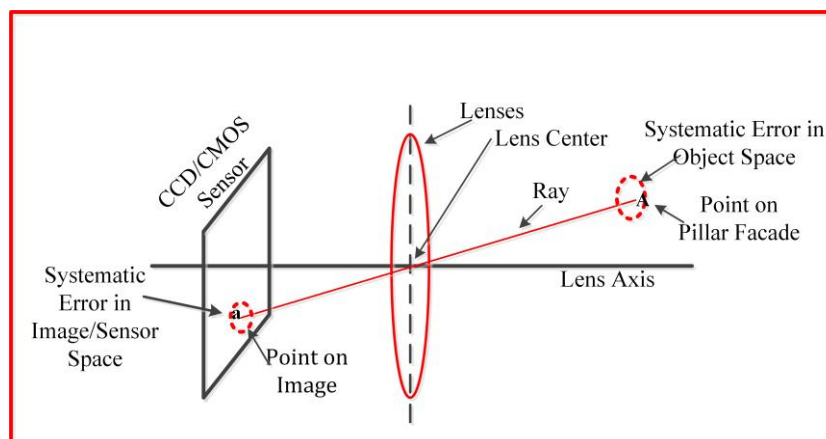


Figure 4. Around 120 retro targets attached to the pillar facade

In this paper, the deformation model is defined as deviations of 3D coordinates vectors of the target points measured in different epochs as seen in (22). Elaborations of about a datum defect or coordinate system differences between two epochs are out of the scope of discussion.

To statistically assess the 3D coordinates, a test of a statistical hypothesis is performed which leads to a decision of whether to accept or reject the hypothesis under consideration. The statistical hypothesis itself is assertion about the distribution of the random variable considered. The statistical test outlined in this paper is premised on that the coordinate observations are normally distributed where statistical interpretation of the displacement test can be undertaken. For example, a statistical hypothesis concerning the observable coordinates of target points is that they follow the normal distribution with a specific mean and variance values that can be inferred into a null hypothesis of  $H_0$  test. The result of that is a statistical decision concerning the validity of  $H_0$  of the postulate value of deformation model.

Referring to Fig. 2, a general simplified two-epoch geometric deformation analysis is performed as follows: First, test on the variance ratio of coordinates of the target points between two epochs. Only if the test is passed the assessment can be continued to the next step. Then transform both coordinate systems of the two of the networks being compared into a common datum defined by the stable reference points. Second, conduct a global congruency test to determine if the object points have been displaced between epochs. If the test is passed, no displacement occurs, and analysis can be stopped here. Otherwise, the next step, local or partial congruency test is performed to quantify individual or group of points displacements within the datum. Last step, perform localization of deformation test to verify that the point movements constitute a statistically significant deformation [67]. The analysis of significant deformations between two epochs is mandatory process since the measured and estimated displacements need to be verified in statistical testing, in which a rejection of the test implied target point movement occurs. Although the analysis includes the four main tests, the adopted procedures do not explicitly proceed in the order given above but rather comprise repeated and interrelated tests between partial congruency testing and localization of single point displacements.

2.2.2. Variance Ratio Test

Prior to the global congruency testing, the test begins with examining null hypothesis whether that the network of object target points is stable over all measuring epochs at significant level of  $\alpha$  (i.e. 5%) by testing the variance ratio of the epoch 1 and the epoch 2 measurements as follows.

$$H_0: \hat{\sigma}_{0_1}^2 = \hat{\sigma}_{0_2}^2 \text{ against } H_1: \hat{\sigma}_{0_1}^2 \neq \hat{\sigma}_{0_2}^2 \quad (19)$$

$$T = \frac{\hat{\sigma}_{0_2}^2}{\hat{\sigma}_{0_1}^2} \sim F_{dof_1, dof_2} \quad (20)$$

$$dof = dof_1 + dof_2 \quad (21a)$$

$$\hat{\sigma}_0^2 = (dof_1 \hat{\sigma}_{0_1}^2) + dof_2 \hat{\sigma}_{0_2}^2 / dof \quad (21b)$$

Where  $\hat{\sigma}_{0_1}^2$  and  $\hat{\sigma}_{0_2}^2$  are the posteriori variance of the self-calibrating bundle adjustment computation in epoch 1 and epoch 2 respectively, assuming the  $\hat{\sigma}_{0_2}^2$  larger than  $\hat{\sigma}_{0_1}^2$ . T is the variance ratio to be tested against a standard F-test (i.e. Fisher distribution) at degrees of freedom of  $dof_1$  and  $dof_2$  of each computation. A failure of the test indicates that it requires further examination of the measurement and the bundle adjustment process [68], and the congruency test must not be continued. If the test is passed the combined degree of freedom of (21a) and the combined variance factor of (21b) are incorporated into the congruency test.

The congruency test is required to analyze a consistency and stability of the point networks given a set of target points in two epochs [8]. If the set of points are all target points in initial assessment, it is called a global congruency test otherwise a local or partial congruency test. All target points between two epochs that are passed during the test are considered as stable datum points.

2.2.3. Global Congruency Test

Global congruency test is applied to all common target points to both epochs. It examines whether significant displacements have occurred between two epochs. If there is a significant movement on a single or some points, the test is failed, then the localization test is followed before commencing a local congruency test on the remaining stable datum points. The test examines null hypothesis  $H_0$  (i.e. no significant movements) of displacement vectors of  $d$  and its cofactor matrix of  $Q_d$  over two epochs which can be formulated as:

$$d = x_2 - x_1 ; Q_d = Q_{x_2} + Q_{x_1} \quad (22)$$

$$H_0: d = 0 \text{ against } H_1: d \neq 0 \quad (23)$$

Where  $x_1$  and  $x_2$  are the vectors of 3D coordinates of the target points in both epochs, and their corresponding cofactor matrix of  $Q_{x_1}$  and  $Q_{x_2}$  must be on the same datum. A standard F-test is used in (23) to test the acceptance of the null hypothesis  $H_0$  against its alternative  $H_1$ . The test is datum independent and expressed as [66,68]:

$$T = \frac{\Omega}{h \hat{\sigma}_0^2} = \frac{d^T Q_d^+ d}{h \hat{\sigma}_0^2} \sim F_{h,dof,1-\alpha} \quad (24)$$

Where  $\hat{\sigma}_0^2$  and  $dof$  are the common variance factor and the sum of degrees of freedom in both epochs computed in (21). The  $h$  is the rank of the cofactor matrix of  $Q_d$  which is equal to  $3n-7$  for the 3D Cartesian coordinate system, where  $n$  is the number of object target points. Also, there is a Moore-Penrose pseudo inverse of  $Q_d^+$  together with its inner constraint matrix  $G$  such that [68]:

$$Q_d^+ = (Q_d + GG^T)^{-1} - G(G^T GG^T G)^{-1} G^T \quad (25)$$

$$\mathbf{G}_i = \begin{bmatrix} 1 & 0 & 0 & 0 & Z_i & -Y_i & X_i \\ 0 & 1 & 0 & -Z_i & 0 & X_i & Y_i \\ 0 & 0 & 1 & Y_i & -X_i & 0 & Z_i \end{bmatrix} \quad (26)$$

The matrix  $\mathbf{G}$  has a dimension of 3 by 7 for any  $i^{\text{th}}$  target point, the provisional coordinates of the first epoch are utilized as centroid to avoid numerical instability.

The test of  $T$  in (24) is against  $F_{h, \text{dof}, 1-\alpha}$ , at significant level of  $\alpha = 0.05$ . The  $F$  follows the central Fisher distribution that verifies the null hypothesis whether the two geometric networks are congruent with the predetermine tolerance of their coordinates precision. If the test passes, the hypothesis that the network has not undergone a change in shape is accepted. If the test fails it is due to the presence of statistically significant point displacements. If  $T$  is less than the critical value of  $< F_{h, \text{dof}, 1-\alpha}$ , the  $H_0$  is accepted and the test passes. There are no significant displacements within the set of the target points and the analysis quits here.

#### 2.2.4. Local or Partial Congruency Test

In contrast, if  $T$  is greater than the critical value,  $H_0$  is rejected, which indicates significant movements. Then it is necessary to further analysis the movements via localization test, followed by the partial congruency test that examines the stability of the retained datum network of target points only as a part of the initial datum. If  $\mathbf{d}$  and  $\mathbf{Q}_d$  can be partitioned as [68]

$$\mathbf{d} = \begin{bmatrix} \mathbf{d}_r \\ \mathbf{d}_e \end{bmatrix}; \mathbf{Q}_d = \begin{bmatrix} \mathbf{Q}_r & \mathbf{Q}_{re} \\ \text{symm} & \mathbf{Q}_e \end{bmatrix} \quad (27)$$

Where the subscripts  $e$  and  $r$  refer to “eliminated” and “retained”. The subscript  $r$  indicates a remaining network of datum points, while the subscript  $e$  refers to non-datum points that are previously eliminated datum points from the computational base. If  $k$  expresses the number of eliminated points, the statistical test of the null hypothesis of the partial congruency test becomes:

$$H_0: E\{\mathbf{d}_r\} = 0 \quad (28)$$

$$T = (\mathbf{d}_r^T \mathbf{Q}_r^+ \mathbf{d}_r) / \hat{\sigma}_0^2 (h - 3k) \sim F_{h-3k, \text{dof}, 1-\alpha} \quad (29)$$

#### 2.2.5. Localization of Deformation Test

When the global congruency test in (24) fails, it indicates significant displacement [8]. It is known that a non-congruency of the network between the two epochs is folded in the quadratic form of  $\Omega$  which is possible to measure the contribution of each point displacement of  $\mathbf{d}_i = [dX \ dY \ dZ]^T$  to the value of  $\Omega_i$ . The point with the largest  $\Omega_i$  is deemed to be significantly displaced. Computation of individual value  $\Omega_i$  is using a partitioning method [66] of both the vector  $\mathbf{d}$  and the pseudoinverse of  $\mathbf{Q}_d^+$  for each target point as follows [68]:

$$\Omega_i = \bar{\mathbf{d}}_i^T P_i \bar{\mathbf{d}}_i \quad (30)$$

$$\bar{\mathbf{d}}_i = P_i^{-1} P_{ri} \mathbf{d}_r + \mathbf{d}_i \quad (31)$$

$$\mathbf{d} = \begin{bmatrix} \mathbf{d}_r \\ \mathbf{d}_i \end{bmatrix}; \mathbf{Q}_d^+ = \begin{bmatrix} P_r & P_{ri} \\ P_{ir}^T & P_i \end{bmatrix} \quad (32)$$

$$\mathbf{d}_i = [dX_i \ dY_i \ dZ_i]^T \quad (33)$$

The computation of (30) is repeated for each point, and the location of the point which contributes most to the largest  $\Omega_i$  of the non-congruency of the network is interactively eliminated. The partial congruency test must be repeated, but the influence of the first located displacement (i.e.  $\mathbf{d}_i$ ) is removed from the common network datum. Every time the point is removed from the computational base, reordering of both vector  $\mathbf{d}$  and covariance matrix  $\mathbf{Q}_d$  is necessary. This reordering strategy is similar to that of (27), including matrix  $\mathbf{G}$  and diagonal matrix  $\mathbf{I}_p$  [68]:

$$\mathbf{d} = \begin{bmatrix} \mathbf{d}_r \\ \mathbf{d}_e \end{bmatrix}; \mathbf{Q}_d = \begin{bmatrix} \mathbf{Q}_r & \mathbf{Q}_{re} \\ \mathbf{Q}_{er} & \mathbf{Q}_e \end{bmatrix}; \mathbf{I}_p = \begin{bmatrix} \mathbf{I}_r \\ \mathbf{I}_e \end{bmatrix}; \mathbf{G} = \begin{bmatrix} \mathbf{G}_r \\ \mathbf{G}_e \end{bmatrix}; \mathbf{d}_e = \mathbf{d}_i = [dX_i \ dY_i \ dZ_i]^T \quad (34)$$

Where  $\mathbf{d}_e$  is the vector of eliminated point formed by the single displacement  $\mathbf{d}_i$  in (30). The  $\mathbf{d}_r$  and  $\mathbf{Q}_r$  refer to the element of remaining datum points,  $\mathbf{Q}_e$  is a 3 by 3 symmetric cofactor matrix for  $\mathbf{d}_e$ . Element of  $\mathbf{I}_r$  corresponding to datum points is set to one, while  $\mathbf{I}_e$  for the non-datum points is set to zero. Matrix  $\mathbf{G}$  is calculated once only and reordered to facilitate the use an S-transformation [66] which utilizes (27) as follows [67]:

$$\mathbf{d}' = \begin{bmatrix} \mathbf{d}'_r \\ \mathbf{d}'_e \end{bmatrix} = \mathbf{S} \mathbf{d}; \mathbf{Q}'_d = \mathbf{S} \mathbf{Q}_d \mathbf{S}^T = \begin{bmatrix} \mathbf{Q}'_r & \mathbf{Q}'_{re} \\ \mathbf{Q}'_{er} & \mathbf{Q}'_e \end{bmatrix} \quad (35)$$

$$\mathbf{S} = [\mathbf{I} - \mathbf{G}(\mathbf{G}^T \mathbf{I}_d \mathbf{G})^{-1} \mathbf{G}^T \mathbf{I}_d] \quad (36)$$

$$\mathbf{S} = \begin{bmatrix} \mathbf{I} - \mathbf{G}_r \mathbf{R} & \mathbf{0} \\ -\mathbf{G}_e \mathbf{R} & \mathbf{I} \end{bmatrix}; \mathbf{R} = (\mathbf{G}_r^T \mathbf{G}_r)^{-1} \mathbf{G}_r^T \quad (37)$$

Where  $\mathbf{G}_r$  and  $\mathbf{G}_e$  are similarity transformation matrices corresponding to  $\mathbf{x}_r$  and  $\mathbf{x}_e$ . The  $\mathbf{G}$  matrix is that which is routinely applied to impose datum constraints in free-network adjustment via inner constraint [67]. Elements of  $\mathbf{I}_d$  are set to one or zero for datum and non-datum points respectively. The S-matrix can be formed by (36) or (37), and vectors  $\mathbf{d}'_r$  and  $\mathbf{d}'_e$  refer to the datum and non-datum points. After this transformation, the partial congruency test is performed again on the retained points to examine whether the vector  $\mathbf{d}'_r$  still contains any further significant displacements. If there are  $k$  removed points in  $\mathbf{d}'_e$ , the partial congruency test is performed as

$$\mathbf{d}'_r^T \mathbf{Q}'_r^+ \mathbf{d}'_r / (h - 3k) \hat{\sigma}_0^2 < F_{h-3k, \text{dof}, 1-\alpha} \quad (38)$$

Where the  $\mathbf{Q}'_r^+$  is the sub-matrix of the pseudo inverse  $\mathbf{Q}'_d^+$  corresponding to  $\mathbf{d}'_r$ . If the test passes, the null hypothesis that the retained network has not changed in shape is accepted. The elements of  $\mathbf{d}'_e$  indicate significant displacements with respect to the stable target point network of  $\mathbf{d}'_r$ . If the partial congruency test fails, the point with the largest component in (30) is added to  $\mathbf{d}'_r$  vector, and  $k$  is incremented by one, the process of partitioning in (31) to (33), reordering in (34), and S-transformation in (35)

to (37) are iterated until the test passes. At the last stage of the localization test, the vectors  $\mathbf{d}$  and  $\mathbf{Q}_d$  in (32) or in (35) as well as contain solution in the form of the partial trace datum that can be used to confirm the localization finding and final testing of the deformation, known as the single point test which is based on the null hypothesis [68]. For a 3D network it becomes

$$\mathbf{d}_i^T \mathbf{Q}_{di}^{-1} \mathbf{d}_i / 3\hat{\sigma}_0^2 < F_{3,dof,1-\alpha} \quad (39)$$

Where  $\mathbf{Q}_{di}$  is the covariance matrix of the displacement vector of  $\mathbf{d}_i$ . The test is conducted for each point. All datum points are expected to be stable, or the displacement vector is negligible.

### 3. Results and Discussion

A two-epoch monitoring campaign was conducted to photograph the susceptible bridge's pillar. In the first epoch, around 300 images were captured to render a 3D perspective view of the DT of all bridge structures as illustrated in Fig. 5. This process was conducted once only. Then, around 10 images of the convergent network were taken separately to measure the coordinate of 66 target points attached to the pillar façade. This pillar measurement was repeated in the second epoch. There are four pillars of the bridge structure that support the entire load on the bridge. Rivers pass through between the second and third pillars. The second one is the object of this study.



Figure 5. A 3D model view of the bridge's digital twin

A 3D model view of the pillar's DT illustrated in Fig. 6 contains retro-target points. But no semantic information has been embedded yet into the BIM model to inform the pillar structure status. However, it clearly shows that the appearance of the target points in the DT model is sharp and vivid.

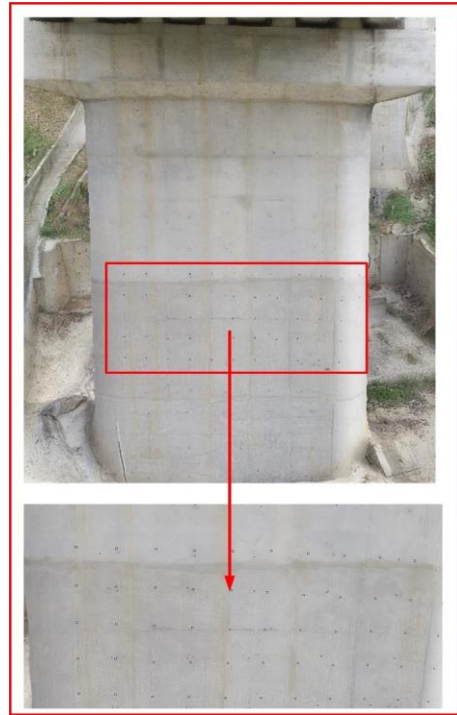


Figure 6. A 3D model view of the pillar's digital twin

Figure 7 shows that all the 66 target points are numbered for identification and image registration process before performing photogrammetric restitution process. The structure over this area needs to be monitored for displacement susceptibility. The camera self-calibrating was performed to compute all the EO and IO parameters, as well as the camera calibration and 3D object target point on both epochs.

The camera self-calibration parameters are shown in Table 1 which consists of the first three IO parameters and nine camera distortion parameters. A Nikon D5200 DSLR camera used in this research has an image resolution of 6000 by 4000 pixels with a pixel size of 0.00392mm. The calibrated focal length of  $c$  and the correction terms of principal point  $(x_0, y_0)$  are varied between two epochs. This proves that the camera is not a resistance proof against the shakes during photography between the two epochs as shown in Fig. 8 for differences on balanced radial distortion profiles. The parameters  $x_0$  and  $y_0$  will rectify the perpendicularity of the lens axis to the CCD/CMOS sensor plane and it also functions as the zero point (datum) for measuring photo coordinates.

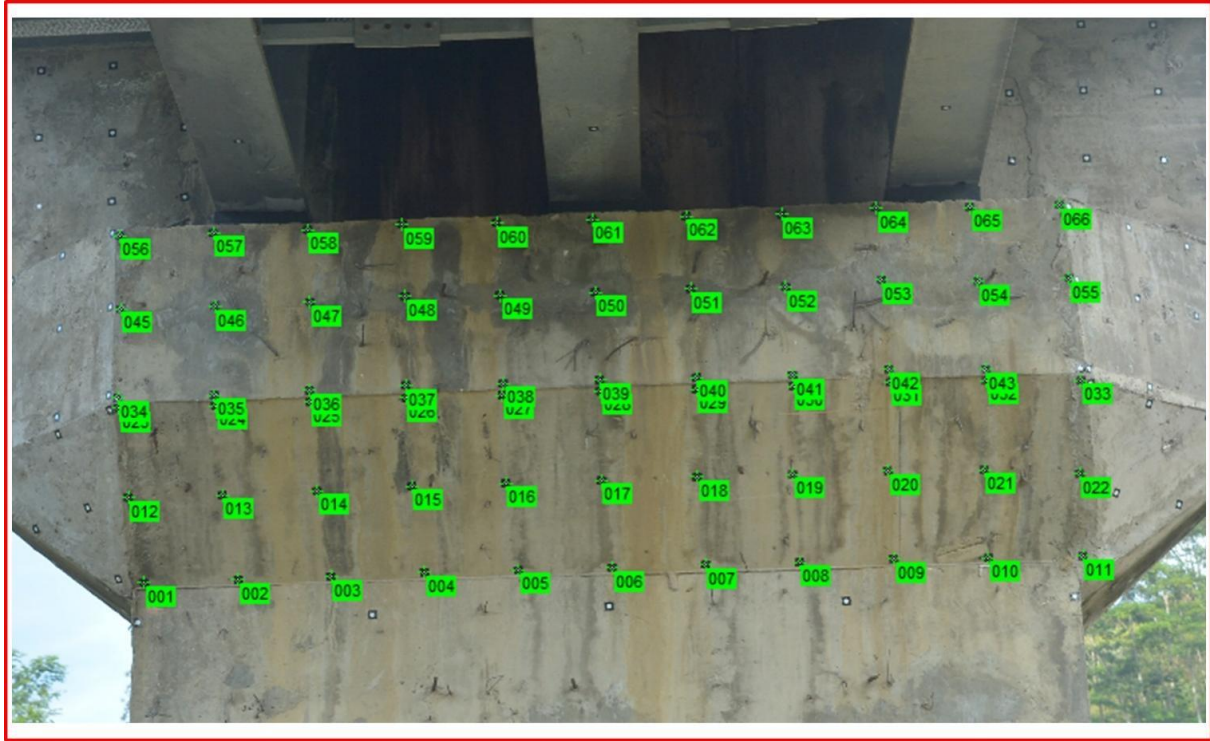
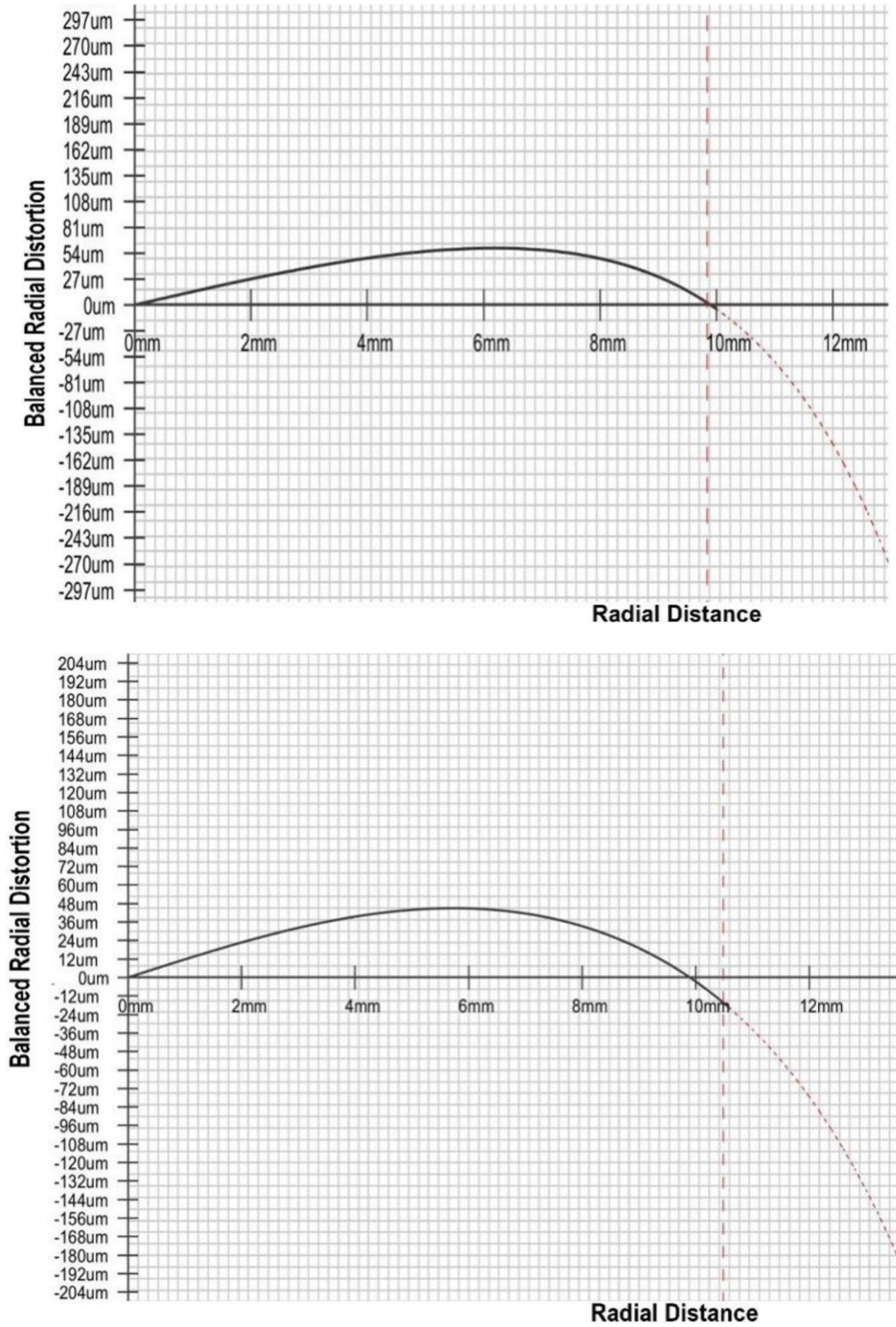


Figure 7. Imaging network of the pillar comprising 66 target points

Table 1. IO and camera distortion parameters on two epochs

Parameters	Epoch 1		Epoch 2	
	values	Standard error	values	Standard error
c (mm)	34.8274	1.03E-02	35.0811	1.16E-02
x <sub>0</sub> (mm)	0.0183	8.85E-03	0.034	7.45E-03
y <sub>0</sub> (mm)	-0.1149	8.86E-03	-0.0894	9.17E-03
K1	3.72E-05	1.70E-06	1.84E-05	2.17E-06
K2	-7.87E-07	2.48E-08	5.04E-08	5.22E-08
K3	7.74E-09	9.79E-11	-2.02E-10	3.98E-10
P1	2.03E-05	2.26E-06	4.10E-06	2.06E-06
P2	3.17E-05	2.27E-06	2.00E-05	2.64E-06
B1	2.43E-33	2.86E-21	2.50E-33	2.31E-21
B2	-2.98E-33	2.86E-21	-3.04E-33	2.31E-21
K4	3.94E-58	2.86E-37	3.94E-58	2.31E-37
K5	1.53E-63	2.86E-41	1.53E-63	2.31E-41



**Figure 8.** Camera balanced radial distortion (in  $\mu\text{m}$ ) compare against Radial Distance (in mm) on epoch 1 (Left) and on epoch 2 (Right)

Table 1 shows the calculation results of 9 parameters of the camera distortion parameters. Parameters K1 – K3 and P1 – P2 are parameters to compensate for lens distortion, namely radial and tangential distortion. These two distortions in the photo will cause straight lines to appear curved. Parameters B1 and B2 will compensate for misalignment, irregularities, and flatness of the CCD/CMOS sensor. The parameters of K4 and K5

compensate for fisheye effect of the lens. These values are almost zero for non-fisheye lens cameras. These nine parameters are used to correct the straightness of the beam/ray line that is deviated by the lens and sensor plane.

These parameters are used to correct the photo coordinates of very retro target points into calibrated photo coordinates. For each shooting session, the accuracy of the photo coordinate measurements can be calculated. The

greater the distortion and noise that can be compensated for, the smaller / more precise the measurement will be. The more precise the photo coordinate measurements, the more precise the coordinate measurements of the retro target points will be, as illustrated in Fig. 4. In other words, the straighter the projection of the line of ray entering the camera lens from the object towards the sensor plane, the more precise the photo coordinate measurements will be and the more precise the calculation of the object's 3D coordinates ultimately.

Table 2 shows the magnitude of the systematic error or RMS values which still contaminate the calibrated photo coordinates. By comparing the calibration parameter data in Table 1, it can be observed that although the calibrated photo coordinates of the retro points have been corrected, there are still systematic errors that cannot be eliminated. These uncompensated systematic errors have not been able to discern and model in the nine calibration parameters. It affects the accuracy of calculated object coordinates and will ultimately affect the value of the minimally detectable magnitude of deformation shifts.

**Table 2.** Uncompensated systematic errors contaminate photo and object target coordinate measurements and imaging network in each epoch

	Epoch 1	Epoch 2
<b>RMS Image coords. (Micron)</b>	0.29	0.24
<b>RMS Object coords. (mm)</b>	0.0465	0.0541
<b>Imaging network scale</b>	1:67700	1:67800
<b>Number of images</b>	10	10
<b>Number of target points</b>	33	33
Degrees of freedom (dof)	460	492

The table also shows that the correlation of accuracy in photo coordinates is comparable to the accuracy of the object coordinates. In general, the image measurement accuracy in epoch 2 is still better than the measurement accuracy in epoch 1. The camera provides sufficient measurement precision of object target coordinates to around 0.046mm and 0.054 in epoch 1 and epoch 2. They would have been zero if there were no distortions occurred. It is understandable that when strong convergent imaging networks of the points are applied, the precision of the network almost reaches a scale of 1:70000. With the large number of *dof* at 460 and 492, 10 images and 33 target points in each epoch; it provides a strong convergent imaging network to enable sub-millimeter precision of the target points measurements that can be figured out in the following Table 3 and Table 4.

**Table 3.** Adjusted 3D coordinates of 33 target points on epoch 1, with their standard error

Point	Coordinates (mm)			Standard errors (mm)		
	X	Y	Z	Sx	Sy	Sz
1	-1354.38	9853.78	-781.19	0.03	0.07	0.03
2	-1059.89	9843.36	-775.90	0.03	0.06	0.03
3	-770.29	9833.13	-769.73	0.03	0.06	0.03
4	-478.04	9819.95	-759.90	0.03	0.06	0.03
5	-186.27	9809.28	-757.04	0.03	0.06	0.03
6	105.14	9797.55	-753.36	0.03	0.07	0.03
7	394.75	9786.16	-746.80	0.03	0.07	0.03
8	686.39	9776.57	-743.67	0.03	0.07	0.03
9	978.31	9766.51	-737.56	0.03	0.06	0.03
10	1271.39	9760.85	-738.98	0.03	0.07	0.03
11	1561.59	9740.55	-736.37	0.04	0.08	0.03
12	-1398.25	9646.41	-196.23	0.03	0.07	0.03
13	-1102.97	9634.35	-192.70	0.03	0.06	0.03
14	-812.17	9626.11	-181.85	0.03	0.06	0.03
15	-518.39	9617.85	-171.06	0.03	0.06	0.03
16	-222.34	9605.67	-170.77	0.03	0.06	0.03
17	70.71	9598.56	-163.70	0.03	0.06	0.03
18	364.51	9588.93	-160.89	0.03	0.07	0.03
19	656.02	9580.60	-157.08	0.03	0.07	0.03
20	948.66	9574.21	-144.35	0.03	0.07	0.03
21	1240.75	9562.27	-149.55	0.03	0.08	0.03
22	1528.46	9559.23	-149.51	0.03	0.08	0.03
23	-1407.69	9845.49	301.02	0.03	0.07	0.03
24	-1114.70	9840.31	304.75	0.03	0.06	0.03
25	-822.53	9835.18	309.52	0.03	0.06	0.03
26	-528.93	9829.79	321.62	0.03	0.06	0.03
27	-236.68	9820.49	322.15	0.03	0.07	0.03
28	60.60	9811.57	326.76	0.03	0.07	0.03
29	350.98	9806.31	332.55	0.03	0.07	0.03
30	645.08	9791.12	333.89	0.03	0.07	0.03
31	938.75	9783.92	350.06	0.03	0.07	0.03
32	1227.21	9771.96	347.60	0.03	0.08	0.03
33	1502.76	9761.07	349.69	0.03	0.08	0.03

**Table 4.** Adjusted 3D coordinates of 33 target points on epoch 2, with their standard error

Point	Coordinates (mm)			Standard errors (mm)		
	X	Y	Z	Sx	Sy	Sz
1	-1354.27	9853.48	-781.40	0.04	0.05	0.05
2	-1059.76	9843.13	-775.93	0.03	0.04	0.04
3	-770.22	9832.98	-769.75	0.03	0.04	0.04
4	-477.98	9819.83	-759.82	0.03	0.04	0.04
5	-186.27	9809.19	-756.95	0.03	0.04	0.04
6	105.14	9797.77	-753.39	0.03	0.04	0.04
7	394.84	9786.36	-746.71	0.03	0.04	0.04
8	686.44	9776.72	-743.57	0.03	0.04	0.04
9	978.20	9767.01	-737.41	0.04	0.04	0.04
10	1271.25	9761.38	-738.82	0.04	0.04	0.04
11	1561.48	9741.23	-736.40	0.04	0.05	0.04
12	-1397.98	9646.72	-196.15	0.04	0.05	0.03
13	-1102.76	9634.07	-192.70	0.04	0.05	0.02
14	-812.05	9626.07	-181.87	0.04	0.05	0.02
15	-518.46	9617.39	-171.09	0.03	0.05	0.02
16	-222.51	9605.61	-170.88	0.03	0.05	0.02
17	70.71	9598.62	-163.77	0.03	0.05	0.02
18	364.84	9588.45	-161.03	0.03	0.05	0.02
19	656.28	9580.39	-157.16	0.03	0.05	0.02
20	948.74	9573.94	-144.41	0.03	0.05	0.02
21	1240.77	9561.76	-149.41	0.04	0.05	0.02
22	1528.88	9557.54	-150.66	0.04	0.06	0.03
23	-1407.51	9846.01	301.09	0.03	0.05	0.04
24	-1114.93	9840.35	304.77	0.03	0.04	0.04
25	-822.63	9835.38	309.71	0.04	0.04	0.04
26	-529.15	9829.74	321.67	0.03	0.05	0.04
27	-236.91	9820.78	322.31	0.03	0.05	0.04
28	60.39	9811.73	326.89	0.03	0.05	0.04
29	350.88	9806.34	332.67	0.03	0.05	0.04
30	644.94	9791.40	334.01	0.03	0.05	0.04
31	938.64	9784.54	350.00	0.13	0.19	0.06
32	1226.94	9772.01	347.69	0.04	0.05	0.04
33	1502.49	9761.19	349.91	0.04	0.05	0.05

Table 3 and Table 4 show the 3D coordinates of the object target points together with their precisions of measurements. However, only 33 out of 66 target points are shown for the purpose of conciseness of the discussion. The range of precision measurements is between 0.03mm to 0.07mm in epoch 1 as well as 0.04mm to 0.05mm in

epoch 2, with the average value being 0.05mm and 0.04mm in epoch 1 and epoch 2 respectively. It shows that homogenous distribution of precision was achieved at each epoch as characterized the convergent imaging network.

In each epoch, photogrammetric restitution was performed to calculate the 3D coordinates of the target points. The S-transformation or 3D similarity seven parameters transformation is utilized to make both coordinate systems in the same datum of computational base. In this case, a datum system in the second epoch is transformed into the datum of the first epoch. Some details of the transformation process are out of the scope of the discussion, but interested readers can refer to [56,60]. After the transformation process, both sets of target point coordinates in Table 3 and Table 4 have the same datum or computational base. The sole purpose of this reason is that a displacement computation vector of  $\mathbf{d}$  and analysis (Table 5) must be conducted within one reference system.

Table 5 shows the 3D displacement vectors of  $\mathbf{dX}$ ,  $\mathbf{dY}$ , and  $\mathbf{dZ}$  as well as the squared root of them in ( $\mathbf{d}$ ) of target points between two epochs as stated in (22) and the value of  $\Omega$  in (24). The minimum detectable displacement occurs at target point of 17 with a value of about 0.09mm. In contrast, the largest deformation occurs at point 22 with a displacement of 2.09mm. Overall, an average of 0.39mm of displacements of all points can be detected. However, we must discern whether the displacement values were from a pure point movement only or they had been contaminated by uncompensated systematic errors. That is the global congruency test role which is handy as illustrated in Table 6.

Table 6 shows the precision measurements of each target point in both epochs as well as the susceptible displacement vectors of each point. Revisiting point 17 that has the smallest value of movement of 0.09mm and considering the measurement precisions of the point are about 0.08mm epoch 1 and 0.06mm epoch 2, it is conclusively stated that the precisions of measurements are better than the magnitude of the smallest susceptible movement. The DSLR camera has a capability of detecting such a small value of the shift in the strong convergent imaging network. On the other hand, the largest movement can be spotted is about 2.09mm at the point 22. Again, the weakest measurement precision occurs at this point, which is 0.1mm at epoch 1.

Table 6 shows that the global congruency test was performed on the network of points. The threshold value of the F-distribution with the parameters of a rank of the  $Q_d$  comprising 33 target points is equal to 92, and the *dof* on both epochs is 952 with significant level of 0.05 being 0.763. Table 6 depicts that the  $\mathbf{T}$  value of each target point is below the threshold value, which means that the null hypothesis is accepted, and all points pass the global congruency test. There are no significant movements within the set of the target points, so the localization test is not necessarily performed.

**Table 5.** Displacement vectors between two epochs

Point	Displacements (mm)				$\Omega$
	dX	dY	dZ	d	
1	0.11	-0.31	-0.20	0.38	5.67E-05
2	0.13	-0.24	-0.04	0.27	2.47E-05
3	0.08	-0.14	-0.02	0.16	8.93E-06
4	0.06	-0.13	0.08	0.16	8.25E-06
5	0.00	-0.09	0.09	0.13	4.94E-06
6	0.00	0.23	-0.03	0.23	2.35E-05
7	0.09	0.20	0.08	0.24	2.17E-05
8	0.05	0.15	0.10	0.19	1.20E-05
9	-0.10	0.50	0.15	0.53	1.12E-04
10	-0.13	0.53	0.16	0.57	1.59E-04
11	-0.11	0.68	-0.03	0.69	3.33E-04
12	0.28	0.31	0.08	0.42	7.26E-05
13	0.21	-0.29	-0.01	0.35	4.62E-05
14	0.13	-0.03	-0.02	0.13	2.71E-06
15	-0.06	-0.46	-0.03	0.47	9.70E-05
16	-0.17	-0.07	-0.11	0.21	6.48E-06
17	0.01	0.06	-0.07	0.09	1.88E-06
18	0.33	-0.49	-0.14	0.60	1.36E-04
19	0.26	-0.21	-0.08	0.35	3.27E-05
20	0.08	-0.27	-0.05	0.29	3.70E-05
21	0.02	-0.50	0.13	0.52	1.63E-04
22	0.43	-1.69	-1.15	2.09	2.33E-03
23	0.19	0.52	0.06	0.56	1.47E-04
24	-0.23	0.05	0.02	0.24	8.04E-06
25	-0.10	0.20	0.19	0.29	2.42E-05
26	-0.22	-0.05	0.05	0.23	7.73E-06
27	-0.23	0.28	0.16	0.40	5.00E-05
28	-0.21	0.16	0.13	0.29	2.19E-05
29	-0.10	0.03	0.12	0.16	4.58E-06
30	-0.14	0.29	0.12	0.34	4.80E-05
31	-0.11	0.62	-0.07	0.63	8.88E-04
32	-0.27	0.05	0.09	0.29	1.45E-05
33	-0.27	0.13	0.21	0.37	3.19E-05

**Table 6.** Congruency test of displacement vectors between two epochs

Point	Precision measurement (mm)		Displacement vector (mm)	T	F-test
	Epoch 1	Epoch 2			
1	0.08	0.08	0.38	2.4E-06	Pass
2	0.07	0.07t	0.27	1.0E-06	Pass
3	0.07	0.07	0.16	3.7E-07	Pass
4	0.07	0.07	0.16	3.5E-07	Pass
5	0.08	0.07	0.13	2.1E-07	Pass
6	0.08	0.07	0.23	9.8E-07	Pass
7	0.08	0.07	0.24	9.1E-07	Pass
8	0.08	0.07	0.19	5.0E-07	Pass
9	0.08	0.07	0.53	4.7E-06	Pass
10	0.09	0.07	0.57	6.7E-06	Pass
11	0.10	0.08	0.69	1.4E-05	Pass
12	0.09	0.07	0.42	3.0E-06	Pass
13	0.08	0.07	0.35	1.9E-06	Pass
14	0.07	0.07	0.13	1.1E-07	Pass
15	0.07	0.06	0.47	4.1E-06	Pass
16	0.07	0.06	0.21	2.7E-07	Pass
17	0.08	0.06	0.09	7.9E-08	Pass
18	0.08	0.06	0.60	5.7E-06	Pass
19	0.08	0.06	0.35	1.4E-06	Pass
20	0.08	0.06	0.29	1.6E-06	Pass
21	0.09	0.07	0.52	6.8E-06	Pass
22	0.10	0.07	2.09	9.8E-05	Pass
23	0.08	0.07	0.56	6.2E-06	Pass
24	0.08	0.07	0.24	3.4E-07	Pass
25	0.07	0.07	0.29	1.0E-06	Pass
26	0.08	0.07	0.23	3.2E-07	Pass
27	0.08	0.07	0.40	2.1E-06	Pass
28	0.08	0.07	0.29	9.2E-07	Pass
29	0.08	0.07	0.16	1.9E-07	Pass
30	0.08	0.07	0.34	2.0E-06	Pass
31	0.08	0.24	0.63	3.7E-05	Pass
32	0.09	0.08	0.29	6.1E-07	Pass
33	0.09	0.08	0.37	1.3E-06	Pass

Apart from the fact that the target points are made of retroreflective material which is attached manually on the bridge's pillar façade, a potential challenge arises to improve the image measurement algorithm to consistently perform precision measurement of coordinate of target points whether there are artificially attached points or not.

Another limitation of this method is that a criteria about strong convergent imaging network. This criterion is intuitively defined based on experience [53] which are usually between  $90^0$  and  $120^0$  of the parallax angles. A weak imaging network would result in non-orthogonal structure of covariance matrices of the coordinates of the

target points, hence the calculation of (25) needs to be performed for all points simultaneously.

To sum up, the interrelated global and partial congruency test as well as the localization of deformation test mechanisms outlined above are sufficient to detect deformation of the bridge structure. However, the procedure of embedding this mechanism onto the DT or BIM model is out of scope of this research. This mechanism is well suited to monitoring bridge structure integrity as it focuses on the localization of single point displacement. It is appealing to propose this method for wider usage. The deformation analysis procedure outlined in this paper requires a well design photogrammetric network utilizing a free-network adjustment that produces a near orthogonal structure of covariance matrices of the coordinates of the target points. It also requires that displacement computation and analysis are calculated on the same computational base, or datum. A convergent photogrammetric network yields homogenous precision of target points as seen in Table 3 and Table 4. The resulting covariance matrix  $Q_x$  of the points can be represented as a block diagonal with 3x3 individual covariance matrix of each point.

## 4. Conclusions

This research shows a convenient and robust method to monitor bridge deformation using a DSLR camera. A sub-millimeter precision of the coordinate measurements is effortlessly attainable. This method readily be integrated with the existing digital twin or BIM model as semantic information for monitoring the bridge's structure integrity. A moderate to strong convergent imaging network is recommended since it can produce a near orthogonal structure of covariance matrices of 3D coordinates which is useful for the simplification of statistical displacement analysis. The orthogonal covariance matrix structures simplify the congruency and localization test procedures. This study demonstrates the effectiveness of using DSLR cameras in capturing detailed displacement data and of using statistical analysis to enable digital twin to simulate self-assessment mechanism to any deformation on bridge structures.

## Acknowledgements

We gratefully thank to Ministry of Research, Technology and Higher Education of the Republic of Indonesia for supporting this research grant based on Decree Number 0667/E5/AL.04/2024 dated 30 May 2024 and Agreement / Contract Number 1091E5/PG.02.AO.PL/2024 dated 1 June 2024; O84|SP2H/P1/LL7 /2024 dated 12 June 2024 with LLDIKTI VII; and with a contract number with ITN Malang: ITN.06.0968.10/IX.REK/2024 dated 13 June

2024.

## REFERENCES

- [1] Z. Wu, G. Chen, Q. Ding, B. Yuan, X. Yang. Three-Dimensional Reconstruction-Based Vibration Measurement of Bridge Model Using UAVs, *Applied Sciences*, Vol.11, No.11, 1-17, 2021. <https://doi.org/10.3390/app11115111>.
- [2] B. A. Kusimba, T. Rinzin, Y. Banno, K. Kinoshita. Condition Assessment and Adaptation of Bailey Bridges as a Permanent Structures, *Applied Sciences*, Vol.12, No.22. 1-24, 2022. <https://doi.org/10.3390/app122211673>.
- [3] X. Li, Y. Xiao, H. Guo, J. Zhang. A BIM Based Approach for Structural Health Monitoring of Bridges, *KSCE Journal of Civil Engineering*, Vol.26, No.1, 155-165, 2022. <https://doi.org/10.1007/s12205-021-2040-3>.
- [4] A. Scianna, G. Fulvio, G. Marcello-La. Structure Monitoring with BIM and IoT: The Case Study of a Bridge Beam Model, *ISPRS International Journal of Geo-Information*, Vol.11, No.3, 1-14, 2022. <https://doi.org/10.3390/ijgi11030173>.
- [5] J. Zhu, N. Luo, Z. Guo, J. Lai, L. Zuo, C. Zhang, Y. Guo, Y. Hu, Feature-constrained automatic geometric deformation analysis method of bridge models toward digital twin, *International Journal of Digital Earth*, Vol.17, No.1, 1-22, 2024. <https://doi.org/10.1080/17538947.2024.2312219>.
- [6] V. Mousavi, M. Rashidi, M. Mohammadi, B. Samali. Evolution of Digital Twin Frameworks in Bridge Management: Review and Future Directions, *Remote Sensing*, Vol.16, No.1887, 1-38, 2024. <https://doi.org/10.3390/rs16111887>.
- [7] J. Moyano, I. Gil-Ariza, J. E. Nieto-Julián, D. Marín-García. Analysis and management of structural deformations through parametric models and HBIM workflow in architectural heritage, *Journal of Building Engineering*, Vol.45, No.103274, 1-18, 2022. <https://doi.org/10.1016/j.jobbe.2021.103274>.
- [8] M. E. Tjahjadi, L. A. Parsamardhani, K. T. Suhari. Bridge Structural Deformation Monitoring Using Digital Camera, *IOP Conference Series: Earth and Environmental Science*, Vol.1051, No.012009, 1-10, 2022. <https://doi.org/10.1088/1755-1315/1051/1/012009>.
- [9] M. K. R. Al-Nasar, F. M. S. Al-Zwainy. A systematic review of structural materials health monitoring system for girder-type bridges, *Materials Today: Proceedings*, Vol.49, A19–A28, 2022. <https://doi.org/10.1016/j.matpr.2021.12.385>.
- [10] A. Spanò, G. Patrucco, G. Sammartano, S. Perri, M. Avena, E. Fillia, S. Milan. Digital Twinning for 20th Century Concrete Heritage: HBIM Cognitive Model for Torino Esposizioni Halls, *Sensors*, Vol.23, No.10. 1-28, 2023. <https://doi.org/10.3390/s23104791>.
- [11] S. C. Jayasinghe, M. Mahmoodian, A. Sidiq, T.M. Nanayakkara, A. Alavi, S. Mazaheri, F. Shahrivar, Z. Sun, S. Setunge. Innovative digital twin with artificial neural

- networks for real-time monitoring of structural response: A port structure case study, *Ocean Engineering*, Vol.312, 1-15, 2024. <https://doi.org/10.1016/j.oceaneng.2024.119187>.
- [12] X. Xu, X. Zhao, H. Yang, I. Neumann. TLS-Based Feature Extraction and 3D Modeling for Arch Structures, *Journal of Sensors*, Vol.2017, 1-8, 2017. <https://doi.org/10.1155/2017/9124254>.
- [13] Detchev, A. Habib, M. El-Badry. Dynamic beam deformation measurements with off-the-shelf digital cameras, *Journal of Applied Geodesy*, Vol.7, No.3, 147-157, 2013.
- [14] Chen, J. Reitz, R. Richstein, K.-U. Schröder, J. Roßmann. IoT-Based SHM Using Digital Twins for Interoperable and Scalable Decentralized Smart Sensing Systems, *Information*, Vol.15, No.121, 1-20, 2024. <https://doi.org/10.3390/info15030121>.
- [15] V. R. Gharehbaghi, E. N. Farsangi, M. Noori, T. Y. Yang, S. Li, A. Nguyen, C. M. Chuquitaype, P. Gardoni, S. Mirjalili. A Critical Review on Structural Health Monitoring: Definitions, Methods, and Perspectives, *Archives of Computational Methods in Engineering*, Vol.29, 2209-2235, 2021. <https://doi.org/10.1007/s11831-021-09665-9>.
- [16] Z. Wang, Z. Zhang, Z. Liu, M. Dezhkam, Y. Zhao. Methods and Applications of Safety Control for Cable Net Structure Considering Spatiotemporal Changes, Sustainability, Vol.15, No.13922, 1-24, 2023. <https://doi.org/10.3390/su151813922>.
- [17] F. N. Catbas, J. A. Cano, F. Luleci, L. C. Walters, R. Michlowitz. On the Generation of Digital Data and Models from Point Clouds: Application to a Pedestrian Bridge Structure, *Infrastructures*, Vol.9, No.6, 1-21, 2024. <https://doi.org/10.3390/infrastructures9010006>.
- [18] A. Avsievich, V. Avsievich, N. Avsievich, D. Ovchinnikov, A. Ivaschenko, Railway Track Stress-Strain Analysis Using High-Precision Accelerometers, *Applied Sciences*, Vol.11, No.11908, 1-17, 2021. <https://doi.org/10.3390/app112411908>.
- [19] M. Mohammadi, M. Rashidi, M. G. Azandariani, V. Mousavi, Y. Yu, B. Samali. Modern damage measurement of structural elements: Experiment, terrestrial laser scanning, and numerical studies, *Structures*, Vol.58, 1-13, 2023. <https://doi.org/10.1016/j.istruc.2023.105574>.
- [20] Q. Wang, X. Cai, Q. Zhang, Y. Wang, X. Tang. Assessment, Prediction, and Mitigation of Metro-Induced Vibrations for an Opera Theatre Adjacent to a Station: A Case Study, *Urban Rail Transit*, Vol.9, No.4, 281-293, 2023. <https://doi.org/10.1007/s40864-023-00201-5>.
- [21] Doytchinov, P. Shore, B. Nicquevert, X. Tonnellier, A. Heather, M. Modena. Thermal effects compensation and associated uncertainty for large magnet assembly precision alignment, *Precision Engineering*, Vol.59, 134-149, 2019. <https://doi.org/10.1016/j.precisioneng.2019.06.005>.
- [22] P. Hope Akwensi, A. Bharadwaj, R. Wang. APC2Mesh: Bridging the gap from occluded building façades to full 3D models, *ISPRS Journal of Photogrammetry and Remote Sensing*, Vol.211, 438-451, 2024. <https://doi.org/10.1016/j.isprs.2024.04.009>.
- [23] P. Wei, C. Li, Z. Jiang, D. Wang. Real-Time Digital Twin of Ship Structure Deformation Field Based on the Inverse Finite Element Method, *Journal of Marine Science and Engineering*, Vol.12, No.257, 1-18, 2024. <https://doi.org/10.3390/jmse12020257>.
- [24] G. T. Roh, N. Vu, C.-H. Jeon, C. S. Shim. Augmented Data-Driven Machine Learning for Digital Twin of Stud Shear Connections, *Buildings*, Vol.14, No.328, 1-28, 2024. <https://doi.org/10.3390/buildings14020328>.
- [25] [25] J. Bien, T. Kaminski, and M. Kuzawa, Taxonomy of non-destructive field tests of bridge materials and structures, *Archives of Civil and Mechanical Engineering*, Vol.19, No.4, 1353-1367, 2019. <https://doi.org/10.1016/j.acme.2019.08.002>.
- [26] X. W. Ye, C. Z. Dong, T. Liu. A Review of Machine Vision-Based Structural Health Monitoring: Methodologies and Applications, *Journal of Sensors*, Vol.2016, 1-10, 2016. <http://doi.org/10.1155/2016/7103039>.
- [27] H. Wang, Z. Xiong, A. Finn, Z. Chaudhry. A context-driven approach to image-based crack detection, *Machine Vision & Applications*, Vol.27, No.7, 1103-1114, 2016. <https://doi.org/10.1007/s00138-016-0779-1>.
- [28] D. Erdenebat, D. Waldmann, F. Scherbaum, N. Teferle. The Deformation Area Difference (DAD) method for condition assessment of reinforced structures, *Engineering Structures*, Vol.155, 315-329, 2018. <https://doi.org/10.1016/j.engstruct.2017.11.034>.
- [29] J.-P. Montillet, W. M. Szeliga, T. I. Melbourne, R. M. Flake, G. Schröck. Critical Infrastructure Monitoring with Global Navigation Satellite Systems, *Journal of Surveying Engineering*, Vol.142, No.4, 1-13, 2016. [https://doi.org/10.1061/\(asce\)su.1943-5428.0000181](https://doi.org/10.1061/(asce)su.1943-5428.0000181).
- [30] Y. Pang, L. Li. Seismic collapse assessment of bridge piers constructed with steel fibers reinforced concrete, *PLoS ONE*, Vol.13, No.7, 1-20, 2018. <https://doi.org/10.1371/journal.pone.0200072>.
- [31] B. Shan, L. Wang, X. Huo, W. Yuan, Z. Xue. A Bridge Deflection Monitoring System Based on CCD, *Advances in Materials Science and Engineering*, Vol.2016, 1-11, 2016. <https://doi.org/10.1155/2016/4857373>.
- [32] G. Zhou, A. Li, J. Li, M. Duan. Structural Health Monitoring and Time-Dependent Effects Analysis of Self-Anchored Suspension Bridge with Extra-Wide Concrete Girder, *Applied Sciences*, Vol.2018, No.8, 1-21, 2018. <https://doi.org/10.3390/app8010115>.
- [33] G. Morgenthal, N. Hallermann, J. Kersten, J. Taraben, P. Debus, M. Helmrich, V. Rodehorst. Framework for automated UAS-based structural condition assessment of bridges, *Automation in Construction*, Vol.97, 77-95, 2019. <https://doi.org/10.1016/j.autcon.2018.10.006>.
- [34] M. Mandirola, C. Casarotti, S. Peloso, I. Lanese, E. Brunesi, I. Senaldi. Use of UAS for damage inspection and assessment of bridge infrastructures, *International Journal of Disaster Risk Reduction*, Vol.72, No.102824, 1-21, 2022. <https://doi.org/10.1016/j.ijdrr.2022.102824>.
- [35] H. Lee, D. Han. Deformation Measurement of a Railroad Bridge Using a Photogrammetric Board without Control Point Survey, *Journal of Sensors*, Vol.2018, 1-10, 2018. <https://doi.org/10.1155/2018/6851252>.
- [36] E. Fathalla, Y. Tanaka, K. Maekawa, A. Sakura.,

- Quantitative Deterioration Assessment of Road Bridge Decks Based on Site Inspected Cracks, *Applied Sciences*, Vol.8, No.7, 1-20, 2018. <https://doi.org/10.3390/app8071197>.
- [37] B. Erol. Evaluation of High-Precision Sensors in Structural Monitoring, *Sensors*, Vol.10, No.12, 10803-10827, 2010. <https://doi.org/10.3390/s101210803>.
- [38] E. Kwak, I. Detchev, A. Habib, M. El-Badry, C. Hughes. Precise Photogrammetric Reconstruction Using Model-Based Image Fitting for 3D Beam Deformation Monitoring, *Journal of Surveying Engineering*, Vol.139, No.3, 143-155, 2013. [https://doi.org/10.1061/\(asce\)su.1943-5428.0000105](https://doi.org/10.1061/(asce)su.1943-5428.0000105).
- [39] Ii. Chounta, C. Ioannidis. High Accuracy Deformation Monitoring of a Concrete Beam using Automatic Photogrammetric Techniques, *FIG Working Week 2012: Knowing to manage the territory, protect the environment, evaluate the cultural heritage*, 1-16, 2012.
- [40] Detchev, A. Habib, F. He, M. El-Badry. Deformation monitoring with off-the-shelf digital cameras for civil engineering fatigue testing, *ISPRS-International Archives of the Photogrammetry, Remote Sensing and Spatial Information Sciences*, Vol.XL, No.5, 195-202, 2014.
- [41] Detchev, A. Habib, M. Mazaheri, D. Lichti. Practical In Situ Implementation of a Multicamera Multisystem Calibration, *Journal of Sensors*, Vol.2018, No.5351863, 1-12, 2018. <https://doi.org/10.1155/2018/5351863>.
- [42] S. Hekimoglu, B. Erdogan, S. Butterworth. Increasing the Efficacy of the Conventional Deformation Analysis Methods: Alternative Strategy, *Journal of Surveying Engineering*, Vol.136, No.2, 53-62, 2010. [https://doi.org/10.1061/\(asce\)su.1943-5428.0000018](https://doi.org/10.1061/(asce)su.1943-5428.0000018).
- [43] S. Abu Dabous, S. Feroz. "Condition monitoring of bridges with non-contact testing technologies, *Automation in Construction*, Vol.116, No.103224, 1-20. 2020. <https://doi.org/10.1016/j.autcon.2020.103224>.
- [44] T. A. Clarke. An analysis of the properties of targets used in digital close range photogrammetric measurement, *Videometrics III*, Vol.2350, 251-262, 1994.
- [45] A. Gaute-Alonso, D. Garcia-Sanchez, Ó. R. Ramos-Gutierrez., Novel method for an optimised calculation of modal analysis of girder bridge decks, *Scientific Reports*, Vol.12, No.1, 1-18, 2022. <https://doi.org/10.1038/s41598-022-16606-4>.
- [46] C. Liang, J. Zhu, J. Zhang, Q. Zhu, J. Lu, J. Lai, J. Wu. A Knowledge-Guided Intelligent Analysis Method of Geographic Digital Twin Models: A Case Study on the Diagnosis of Geometric Deformation in Tunnel Excavation Profiles, *ISPRS International Journal of Geo-Information*, Vol.13, No.3, 1-17, 2024. <https://doi.org/10.3390/ijgi13030078>.
- [47] Y. Tan, S. Li, H. Liu, P. Chen, Z. Zhou. Automatic inspection data collection of building surface based on BIM and UAV, *Automation in Construction*, Vol.131, No.103881, 1-16, 2021. <https://doi.org/10.1016/j.autcon.2021.103881>.
- [48] X. Zhang, P. Zhao, Q. Hu, M. Ai, D. Hu, J. Li. A UAV-based panoramic oblique photogrammetry (POP) approach using spherical projection, *ISPRS Journal of Photogrammetry and Remote Sensing*, Vol.159, 198-219, 2020. <https://doi.org/10.1016/j.isprsjprs.2019.11.016>.
- [49] C. Stöcker, F. Nex, M. Koeva, M. Gerke. High-Quality UAV-Based Orthophotos for Cadastral Mapping: Guidance for Optimal Flight Configurations, *Remote Sensing*, Vol.12, No.21, 1-23, 2020. <https://doi.org/10.3390/rs12213625>.
- [50] S. Paneru, I. Jeelani. Computer vision applications in construction: Current state, opportunities & challenges, *Automation in Construction*, Vol.132, No.103940, 1-17, 2021. <https://doi.org/10.1016/j.autcon.2021.103940>.
- [51] V. K. Reja, K. Varghese, Q. P. Ha. Computer vision-based construction progress monitoring, *Automation in Construction*, Vol.138, No.104245, 1-12, 2022. <https://doi.org/10.1016/j.autcon.2022.104245>.
- [52] G. Esposito, G. Mastrococco, R. Salvini, M. Oliveti, P. Starita, Application of UAV photogrammetry for the multi-temporal estimation of surface extent and volumetric excavation in the Sa Pigada Bianca open-pit mine, Sardinia, Italy, *Environmental Earth Sciences*, Vol.76, No.3, 1-16, 2017. <https://doi.org/10.1007/s12665-017-6409-z>.
- [53] C. S. Fraser. *Network Design, Close Range Photogrammetry and Machine Vision*, Whittles Publishing, Scotland, UK, 256-281, 2001
- [54] C. S. Fraser. Network Orientation Models for Image-Based 3D Measurement, *International Archives of Photogrammetry and Remote Sensing & Spatial Information Science*, Vol.36, No.5, 1-9, 2005.
- [55] T. Luhmann, C. Fraser, H.-G. Maas. Sensor modelling and camera calibration for close-range photogrammetry, *ISPRS Journal of Photogrammetry and Remote Sensing*, Vol.115, 37-46, 2016. <https://doi.org/10.1016/j.isprsjprs.2015.10.006>.
- [56] C. S. Fraser. Automatic camera calibration in close range photogrammetry, *Photogrammetric Engineering & Remote Sensing*, Vol.79, No.4, 381-388, 2013.
- [57] R. Wackrow, J. H. Chandler. A convergent image configuration for DEM extraction that minimises the systematic effects caused by an inaccurate lens model, *Photogrammetric Record*, Vol.23, No.121, 6-18, 2008. <https://doi.org/10.1111/j.1477-9730.2008.00467.x>.
- [58] C. S. Fraser. Digital camera self-calibration, *ISPRS Journal of Photogrammetry and Remote Sensing*, Vol.52, No.4, 149-159, 1997. [https://doi.org/10.1016/S0924-2716\(97\)00005-1](https://doi.org/10.1016/S0924-2716(97)00005-1).
- [59] B. Altena, T. Goede. Assessing UAV platform types and optical sensor specifications, *ISPRS Annals of the Photogrammetry, Remote Sensing and Spatial Information Sciences*, Vol.2, No.5, 17-24, 2014. <https://doi.org/10.5194/isprannals-II-5-17-2014>.
- [60] S. I. Granshaw. Bundle Adjustment Methods in Engineering Photogrammetry, *Photogrammetric Record*, Vol.10, No.56, 181-207, 1980.
- [61] S. Urban, S. Wursthorn, J. Leitloff, S. Hinz. MultiCol Bundle Adjustment: A Generic Method for Pose Estimation, Simultaneous Self-Calibration and Reconstruction for Arbitrary Multi-Camera Systems, *International Journal of Computer Vision*, Vol.121, No.2, 234-252, 2017. <https://doi.org/10.1007/s11263-016-0935-0>.

- [62] M. E. Tjahjadi. A fast and stable orientation solution of three cameras-based UAV imageries, *ARPN Journal of Engineering and Applied Sciences*, Vol.11, No.5, 3449–3455, 2016. [http://www.arnpjournals.org/jeas/research\\_papers/rp\\_2016/jeas\\_0316\\_3830.pdf](http://www.arnpjournals.org/jeas/research_papers/rp_2016/jeas_0316_3830.pdf)
- [63] M. E. Tjahjadi, F. D. Agustina. Fast and stable direct relative orientation of UAV-based stereo pair, *International Journal of Advances in Intelligent Informatics*, Vol.5, No.1, 24-39, 2019. <https://doi.org/10.26555/ijain.v5i1.327>.
- [64] G. Guillet, T. Guillet, L. Ravanel. Camera orientation, calibration and inverse perspective with uncertainties: A Bayesian method applied to area estimation from diverse photographs, *ISPRS Journal of Photogrammetry and Remote Sensing*, Vol.159, 237–255, 2020. <https://doi.org/10.1016/j.isprsjprs.2019.11.013>.
- [65] N. Bärnin, P. Grussenmeyer. Bundle Adjustment With and Without Damping, *Photogrammetric Record*, Vol.28, No.144, 396–415, 2013. <https://doi.org/10.1111/phor.12037>.
- [66] C. S. Fraser, L. Gruendig. The Analysis of Photogrammetric Deformation Measurements on Turtle Mountain, *Photogrammetric Engineering & Remote Sensing*, Vol.51, No.2, 207-216, 1985.
- [67] C. S. Fraser. Periodic Inspection of Industrial Tooling by Photogrammetry, *Photogrammetric Engineering And Remote Sensing*, Vol.54, No.2, 211–216, 1988.
- [68] H. Setan. A Flexible Analysis Procedure for Geometrical Detection of Spatial Deformation, *Photogrammetric Record*, Vol.15, No.90, 841–861, 1997. <http://www.blackwell-synergy.com/links/doi/10.1111/0031-868X.00095/abs>.
- [69] B. A. King. Some Considerations for the Statistical Testing of Least Squares Adjustments of Photogrammetric Bundles, *The Photogrammetric Record*, Vol.15, No.90, 929–935, 1997. <https://doi.org/10.1111/0031-868X.00102>.
- [70] H. Velsink. On the deformation analysis of point fields, *Journal of Geodesy*, Vol.89, No.11, 1071–1087, 2015. <https://doi.org/10.1007/s00190-015-0835-z>.
- [71] A. Cüneyt. Power of Global Test in Deformation Analysis, *Journal of Surveying Engineering*, Vol.138, No.2, 51–56, 2012. [https://doi.org/10.1061/\(ASCE\)SU.1943-5428.0000064](https://doi.org/10.1061/(ASCE)SU.1943-5428.0000064).